

Electric field dependence of spin qubit in a Si-MOS quantum dot

Rong-Long Ma(马荣龙), Ming Ni(倪铭), Yu-Chen Zhou(周雨晨), Zhen-Zhen Kong(孔真真), Gui-Lei Wang(王桂磊), Di Liu(刘頔), Gang Luo(罗刚), Gang Cao(曹刚), Hai-Ou Li(李海欧), and Guo-Ping Guo(郭国平)

Citation: Chin. Phys. B, 2024, 33 (**6**): 060312. DOI: 10.1088/1674-1056/ad3812
Journal homepage: http://cpb.iphy.ac.cn; http://iopscience.iop.org/cpb

What follows is a list of articles you may be interested in

Design of a novel hybrid quantum deep neural network in INEQR images classification

Shuang Wang(王爽), Ke-Han Wang(王柯涵), Tao Cheng(程涛), Run-Sheng Zhao(赵润盛), Hong-Yang Ma(马鸿洋), Shuai Guo(郭帅)

Chin. Phys. B, 2024, 33 (**6**): 060310. DOI: 10.1088/1674-1056/ad342e

Mobility edges and localization characteristics in one-dimensional quasiperiodic quantum walk

Xin-Hui Cui(崔鑫辉), Hui-Min Wang(王慧敏), and Zhi-Jian Li(李志坚)

Chin. Phys. B, 2024, 33 (**6**): 060301. DOI: 10.1088/1674-1056/ad342d

An anti-aliasing filtering of quantum images in spatial domain using a pyramid structure

Kai Wu(吴凯), Rigui Zhou(周日贵), and Jia Luo(罗佳)

Chin. Phys. B, 2024, 33 (**5**): 050305. DOI: 10.1088/1674-1056/ad2504

Electrical manipulation of a hole ‘spin’-orbit qubit in nanowire quantum dot: The nontrivial magnetic field effects

Rui Li(李睿) and Hang Zhang(张航)

Chin. Phys. B, 2023, 32 (**3**): 030308. DOI: 10.1088/1674-1056/ac873b

Detection of spin current through a quantum dot with Majorana bound states

Ning Wang(王宁), Xingtao An(安兴涛), and Shuhui Lv(吕树慧)

Chin. Phys. B, 2021, 30 (**10**): 100302. DOI: 10.1088/1674-1056/abff1c

---

Electric field dependence of spin qubit in a Si-MOS quantum dot

Rong-Long Ma(马荣龙)[1,2,†], Ming Ni(倪铭)[1,2,†], Yu-Chen Zhou(周雨晨)[1,2], Zhen-Zhen Kong(孔真真)[3], Gui-Lei Wang(王桂磊)[3,4,5], Di Liu(刘頓)[1,2], Gang Luo(罗刚)[1,2], Gang Cao(曹刚)[1,2,5], Hai-Ou Li(李海欧)[1,2,5,‡], and Guo-Ping Guo(郭国平)[1,2,5,6]

[1] *CAS Key Laboratory of Quantum Information, University of Science and Technology of China, Hefei* 230026, *China*
[2] *CAS Center for Excellence in Quantum Information and Quantum Physics, University of Science and Technology of China, Hefei* 230026, *China*
[3] *Key Laboratory of Microelectronics Devices and Integrated Technology, Institute of Microelectronics, Chinese Academy of Sciences, Beijing* 100029, *China*
[4] *Beijing Superstring Academy of Memory Technology, Beijing* 100176, *China*
[5] *Hefei National Laboratory, University of Science and Technology of China, Hefei* 230088, *China*
[6] *Origin Quantum Computing Company Limited, Hefei* 230026, *China*

(Received 5 March 2024; revised manuscript received 22 March 2024; accepted manuscript online 27 March 2024)

Valley, the intrinsic feature of silicon, is an inescapable subject in silicon-based quantum computing. At the spin–valley hotspot, both Rabi frequency and state relaxation rate are significantly enhanced. With protection against charge noise, the valley degree of freedom is also conceived to encode a qubit to realize noise-resistant quantum computing. Here, based on the spin qubit composed of one or three electrons, we characterize the intrinsic properties of valley in an isotopically enriched silicon quantum dot (QD) device. For one-electron qubit, we measure two electric-dipole spin resonance (EDSR) signals which are attributed to partial occupation of two valley states. The resonance frequencies of two EDSR signals have opposite electric field dependences. Moreover, we characterize the electric field dependence of the upper valley state based on three-electron qubit experiments. The difference of electric field dependences of the two valleys is 52.02 MHz/V, which is beneficial for tuning qubit frequency to meet different experimental requirements. As an extension of electrical control spin qubits, the opposite electric field dependence is crucial for qubit addressability, individual single-qubit control and two-qubit gate approaches in scalable quantum computing.

Keywords: silicon-based quantum computing, valley, electric-dipole spin resonance

PACS: 03.67.Lx, 03.67.–a, 68.65.Hb **DOI:** 10.1088/1674-1056/ad3812

1. Introduction

Based on the Loss and DiVincenzo's proposal,[1] a qubit encoded by the electron spin freedom in the gate-defined semiconductor QD device is booming developed.[2–5] Benefiting from the isotopically purified technique[6] and compatibility with available silicon microelectronic fabrication methods,[7–10] silicon has been a promising platform for quantum information processing. A long dephasing time up to 120 μs,[11] single-qubit gate fidelity exceeding 99.9%,[12] two-qubit gate fidelity exceeding 99%,[13–15] and quantum error correction protocol[16] have been demonstrated in recent years.

The electron spin qubit definition requires excellent discrete orbital states. In bulk silicon, the valley states exhibit sixfold degeneracy.[17] Conversely, the sixfold valley degeneracy is lifted by the large in-plane strain where the energy of z valleys is approximately tens of meV below the in-plane valleys.[18,19] The remaining twofold degenerate z valleys are separated by valley splitting ($E_{\rm vs}$) of tens to hundreds of μeV under a vertical electric field and the sharp potential of the interface in QD devices.[19–22] Therefore, a single electron in the lowest valley state is used to encode spin qubit.[11,23]

As an intrinsic feature of spin qubit in silicon QD, the presence of valleys is a mixed blessing. The valley degree of freedom is conceived to encode qubit with protection against charge noise.[24–26] When the Zeeman splitting energy is comparable to $E_{\rm vs}$, the electron spin state and valley state will mix, achieving a significantly enhanced Rabi frequency at this spin–valley hotspot.[27,28] However, the spin state relaxation rate is also enhanced at spin–valley hotspot.[20,29,30] Additionally, due to the presence of valleys, the EDSR signal of a single electron spin qubit in a QD may be more complex than that suggested by the simple two-level Hamiltonian.[23,31] Therefore, a deep understanding of valley is essential for silicon-based quantum computing.

In this paper, we study the electric field dependent characteristics of z valleys based on one-electron (ground valley) and three-electron (upper valley) qubits in a silicon metal–oxide–semiconductor (Si-MOS) QD device. For the ground valley, the electric field dependence of the one-electron qubit resonance frequency is 22.23 MHz/V, and that of the upper valley is −26.21 MHz/V, which is consistent with the result of −29.79 MHz/V extracted from the three-electron qubit in the upper valley state. For scalable quantum computing, if

[†] These authors contributed equally to this work.
[‡] Corresponding author. E-mail: haiouli@ustc.edu.cn

© 2024 Chinese Physical Society and IOP Publishing Ltd

the electron spin qubit is sequentially encoded in the ground and upper valleys, the opposite electric field dependence of the resonance frequency is a significant approach for qubit addressability,[11,32] individual single-qubit control[10,33] and two-qubit gates.[34,35] Furthermore, we characterize the basic properties of one-electron qubit. The suitable Rabi frequency is 2.084 MHz where the microwave (MW) amplitude has little effect on the control quality. The dephasing time of 1.084 μs is measured by the Ramsey fringe, and the coherence time can be enlarged to 191.96 μs by using the Hahn-echo technique.

2. Device and qubit state readout

Figure 1(a) presents the gate defined double quantum dot (DQD) device fabricated on an isotopically purified ^{28}Si epilayer (with the residual ^{29}Si concentration of 60 ppm). Three overlapping layers of aluminum gates[30,36] with plasma enhanced oxidation[37] to ensure electrical isolation property are used to define the QD structure and single-electron-transistor (SET) structure. The device fabrication details can be found in Refs. [30,38–40]. Here, two QDs labelled LD and MD are formed under gates LP and M to store electrons, and we only focus on the electron spin qubit in LD here. The SET structure is capacitively coupled to DQD, and is used to monitor the electron tunneling events to realize qubit state readout via Elzerman readout.[41–43] Beside the aluminum gates, a rectangular micro-magnet (MM, Ti/Co 10/240 nm) is deposited around the QD structure to provide the magnetic field gradient for EDSR.[12,23,44] An external magnetic field $B_{\rm ext}$ provides Zeeman splitting between electron spin states and fully magnetizes the MM.[45] Figure 1(b) shows the cross-section schematic of the DQD structure along the white dashed line in Fig. 1(a). The aluminum gates create confinement potentials to trap electrons in two QDs. Two electron reservoirs accumulate under gates LL and RL, where the right reservoir is extended to gate RB. Therefore, the tunneling rates between two QDs and the electron reservoirs are modified by adjusting the voltages on gates LB and RP, respectively. A bias-tee is connected to the gate LP to deliver the pulse sequence and MW signals simultaneously to control the energy level and realize EDSR.

The typical charge stability diagram of DQD is shown in Fig. 1(c), as measured by monitoring the capacitively coupled SET current $I_{\rm S}$ based on the lock-in amplifier.[38,46] Each QD can be depleted to the last electron individually. Here, we choose $(0,0)$–$(1,0)$ and $(2,0)$–$(3,0)$ charge transitions as the working areas for one-electron and three-electron qubit experiments, where (N_1,N_2) are the numbers of electrons in LD and MD, respectively. For the three-electron qubit experiment, the first two electrons occupy the ground valley to form a singlet state, which has no effect on the third electron.[47] A multi-electron qubit is thought to screen electrical noise to improve the qubit control fidelity.[48,49]

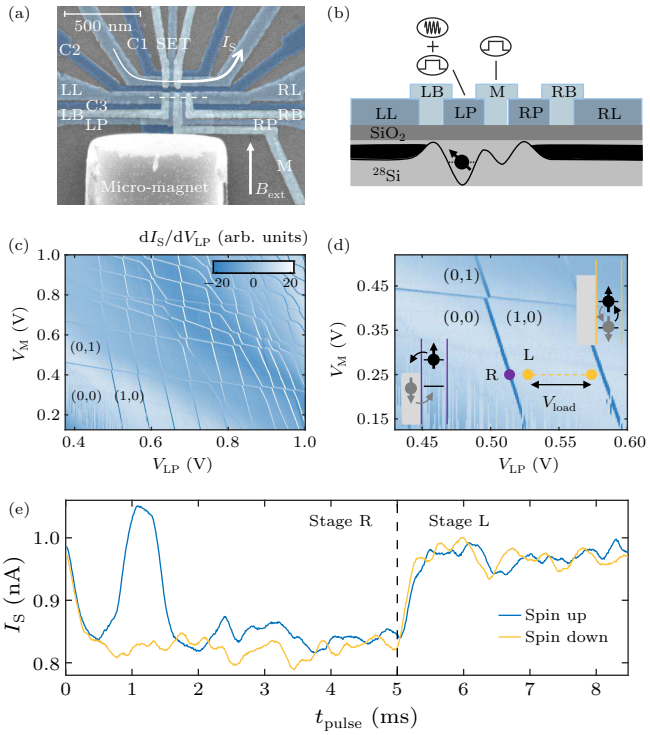


Fig. 1. (a) False-colored scanning electron microscope image of the DQD device nominally identical to that used in the experiment. Three layers of aluminium gates are used to define the DQD structure and tune the experimental parameters. A capacitively coupled SET structure is used as the charge sensor to monitor the electron occupancy of DQD. The MM structure improves the stray magnetic field for qubit state operation. The white arrow indicates the direction of the external magnetic field $B_{\rm ext}$. (b) Cross-section schematic of the DQD structure along the white dashed line in panel (a). Two QDs are confined under gates LP and M, while gates LB and RP are used to control the tunneling rates between QD and its adjacent electron reservoir. Two electron reservoirs accumulate under gates LL and RL, and the right one is extended to gate RB. (c) Charge stability diagram of DQD obtained by sweeping gate voltage $V_{\rm LP}$ and $V_{\rm M}$. The $(0,0)$–$(1,0)$ and $(2,0)$–$(3,0)$ transitions are chosen as the working areas for one-electron and three-electron qubit experiments, respectively. (d) Charge stability diagram around $(0,0)$–$(1,0)$ charge transition line to illustrate the electron state control (point L) and readout (point R) processes, and the measurement approach of electric field dependence of $f_{\rm res}$. The corresponding energy diagram is shown in the inset. (e) Two experimental single-shot traces of the spin up (blue) and spin down (orange) states as a function of pulse sequence time $t_{\rm pulse}$. By monitoring the sudden change of $I_{\rm S}$ shown in the blue trace, the electron spin state can be distinguished.

In Fig. 1(d), we introduce the qubit state control (point L) and readout (point R) processes around the $(0,0)$–$(1,0)$ charge transition, and how to measure the electric field dependence of the qubit resonance frequency $f_{\rm res} = g\mu_{\rm B}B/h$, where g is the electron g-factor, $\mu_{\rm B}$ is the Bohr magneton, h is the Plank's constant and B is the sum magnetic field of $B_{\rm ext}$ and MM is the magnetic field component that parallels to $B_{\rm ext}$. For the qubit state control process (the energy diagram is shown in the right inset of Fig. 1(d)), the initialized spin down electron is pushed deep into the Coulomb blockade region and the resonant MW signal drives the electron wavefunction to move back and forth in the stray magnetic field to obtain a local alternating magnetic field $B_{\rm ac}$,[12,50] which is proportional to the spin flip speed. During the readout process, the Fermi level of

the reservoir lies between the electron spin up and spin down states (see the left inset of Fig. 1(d)). Therefore, if the electron state is spin up, it can tunnel into the adjacent electron reservoir, and a spin down electron will tunnel back to QD after waiting for some time, resulting in a sudden change of I_S (see the blue trace shown in Fig. 1(e)). On the contrary, if the electron state is spin down, there is no tunneling event, indicating that I_S remains unchanged (see the orange trace shown in Fig. 1(e)). By monitoring the sudden change of I_S, the electron spin state can be distinguished.[43] With the ability to operate and read out qubits, we turn to characterize the valley properties of the electric field dependence. When we focus on the electric field dependence of f_{res}, we scan the voltage of the qubit control process (V_{load}) along the orange dotted line in Fig. 1(d) to measure the change in f_{res}.

3. Electric and magnetic field dependence of one-electron qubit

Figure 2(a) shows two closely spaced EDSR signals separated by 28.43 MHz at $B_{ext} = 823$ mT, where two f_{res} are 26.04840 GHz and 26.07683 GHz, respectively. We propose that the bimodal signal corresponds to the spin flip of the electron that occupies the ground valley or the upper valley state. The energy levels of the two lowest valley states and the corresponding qubit state operation processes as a function of B are visualized in Fig. 2(b). Two Zeeman splittings with similar energies $E_Z^{G/U}$ belong to different valley states (the superscripts refer to the ground and upper valley states) and the energy difference between two identical spin states is E_{vs}. Here, the color-coded qubit state operation processes shown in Fig. 2(b) are the same as those in Fig. 2(a), where the larger f_{res} of the bimodal signal corresponds to the ground valley, labeled f_G and the other EDSR signal (labeled f_U) is associated with the upper valley. In the following, we focus on these two intra-valley spin flip processes and provide the basis for classifying two EDSR signals.

For a constant B_{ext}, we scan microwave frequency f_{MW} to measure the bimodal EDSR signal to track f_G and f_U. Then, a set of f_G and f_U as a function of B_{ext} is obtained as shown in Fig. 2(c). The magnetic field dependence of f_{res}, i.e., the electron g-factor of $g_G = 2.13073$ and $g_U = 2.13217$ is extracted. The relative difference, defined as $2(g_U - g_G)/(g_U + g_G)$, is 0.0676%. According to the results of Takura *et al.*,[51] the unperturbed Zeeman splitting E_Z^0 will be renormalized in the presence of a stray magnetic field, and the renormalized Zeeman splitting is $E_Z^0(1 - \frac{0.5M^2}{\Delta^2 - (E_Z^0)^2})$. There are two possible mechanisms to explain the difference of g-factor. The first is the stray magnetic field of MM, where the spin up state of the ground orbit and the spin down state of the first excited orbit are mixed,[51] resulting in the perturbation matrix element $M \sim g\mu_B b_{sl} L$. Here, b_{sl} is the magnetic field gradient of MM, and L is the QD diameter. The other is orbital energy splitting Δ. Due to valley–orbit coupling, Δ is different for the two valley states,[52] and this disorder will enhance the difference of Δ.[53] Therefore, the Zeeman splitting of two valley states is renormalized due to the effect on M and Δ.

Figure 2(d) plots the electric field dependence of f_{res} as a function of the load depth during the qubit state control process, V_{load}. Similar to the magnetic field dependence, the variations in f_G and f_U with V_{load} are extracted by scanning f_{MW}, and the electric field dependence of two valleys are $\alpha_G = 22.23$ MHz/V and $\alpha_U = -26.21$ MHz/V. The opposite signs of α_G and α_U are from the mixture of the out-plane and in-plane motion caused by the in-plane B_{ext}.[49] Furthermore, the different signs of α_G and α_U indicate that the f_{res} of two adjacent qubits encoded in the ground and upper valley states can be simply tuned to be close or further away, which is significant for qubit addressability,[11,32] individual single-qubit control[10,33] and two-qubit gate[34,35] approaches in scalable quantum computing.

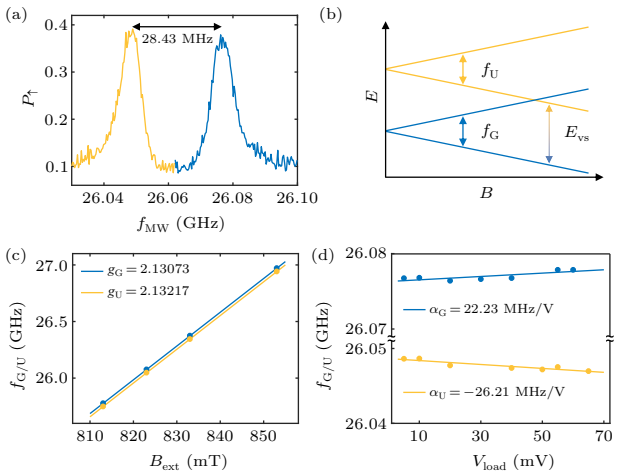


Fig. 2. (a) The bimodal EDSR signals separated by 28.43 MHz at $B_{ext} = 823$ mT, where two f_{res} are 26.04840 GHz and 26.07683 GHz, respectively. The spin flip processes correspond to the transition marked in panel (b). (b) The energy levels of two lowest valley states and the corresponding qubit state operation processes labeled f_G and f_U as a function of B. (c) Magnetic field dependence of f_G and f_U, where the g-factor of two valleys is extracted: $g_G = 2.13073$ and $g_U = 2.13217$. (d) Electric field dependence of f_G and f_U. The opposite dependence of two valleys is $\alpha_G = 22.23$ MHz/V and $\alpha_U = -26.21$ MHz/V.

The bimodal signal is identified as an electron occupying in the ground valley or the upper valley state due to the thermal population. In the Si/SiGe QD platform,[23,54] E_{vs} may be smaller than the thermal energy ($k_B T_e$, where k_B is the Boltzmann constant and T_e is the electron temperature), and a thermally populated process is possible. However, in the Si-MOS QD device here, E_{vs} is approximately 327.3 μeV, and T_e is 258.4 mK corresponding to a thermal energy of 22.3 μeV (see Appendix A for more details). The explanation for thermally populated process does not make sense. Therefore, besides

the basic property characterization of the one-electron qubit in Section 4, the electric field dependence of the upper valley in Fig. 2(d) will be further confirmed in Section 5 based on the three-electron qubit.

4. One-electron qubit properties

After characterizing the electric and magnetic field dependence of two valleys, we study the one-electron qubit properties. Here, we focus on the one-electron qubit that occupies the ground valley (there is no Rabi oscillation of the spin qubit in the upper valley). Figure 3(a) plots the oscillated electron spin up state probability $P_\uparrow$ as a function of duration time $t_{\rm dur}$ of the MW signal when $f_{\rm MW}$ is resonant with $f_{\rm G}$. The experimental data are shown as blue circles, and the black solid line represents the fit with an exponentially damped sinusoidal function. Here, the Rabi frequency $f_{\rm Rabi}$ is 2.804 MHz at the MW power P of 15 dBm, and the quality factor Q, defined as the number of operations during the Rabi decay time, is approximately 18. Figure 3(b) shows the power dependence of $f_{\rm Rabi}$ and Q. $f_{\rm Rabi}$ increases with increasing P, while Q changes from increasing to decreasing at $P = 15$ dBm. We attribute this to the MM structure, where the small transverse magnetic field and large longitudinal magnetic field of MM used here result in a small $f_{\rm Rabi}$ and a fast decay rate. Therefore, for the following Ramsey fringe and dynamic decoupling experiments, we choose $P = 15$ dBm to achieve a balance between the control speed and quality.

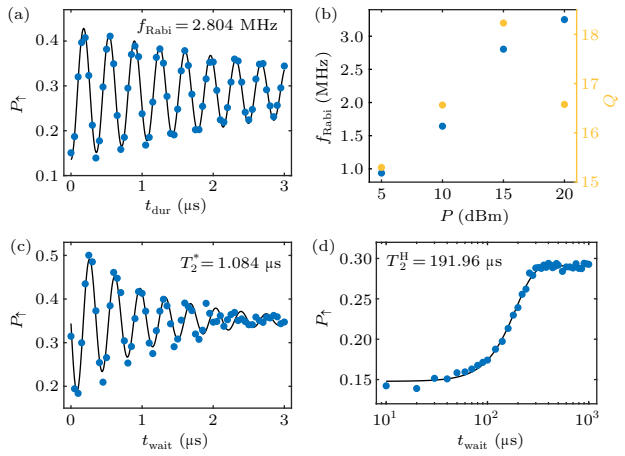


Fig. 3. (a) Electron spin up probability $P_\uparrow$ as a function of $t_{\rm dur}$. The blue circles represent the experimental data and the black solid line is the fit, where the Rabi frequency of 2.804 MHz at $P = 15$ dBm is extracted. (b) MW power dependence of Rabi frequency $f_{\rm Rabi}$ and quality factor Q. $P = 15$ dBm is chosen for the Ramsey fringe and dynamic decoupling experiments. (c) Ramsey fringe results. The dephasing time T_2^* of 1.084 μs is obtained from the fitted black solid line. (d) Hahn-echo measurement results. The qubit coherence time is enlarged to 191.96 μs.

The Ramsey fringe experiment consists of two $\pi/2$ operations that are separated by a wait time $t_{\rm wait}$. The initialized spin down state is operated to the equatorial plane of the Bloch sphere by the first $\pi/2$ operation. During $t_{\rm wait}$, a phase error accumulates due to the fluctuation of $f_{\rm G}$, and the second $\pi/2$ will project the phase error to the z-axis of the Bloch sphere to make it quantifiable. Figure 3(c) plots the Ramsey fringe where $f_{\rm MW}$ is offset by 3 MHz relative to $f_{\rm G}$, and a dephasing time T_2^* of 1.084 μs is extracted. To further improve the qubit coherence time, we employ the dynamic decoupling protocol. Based on the Ramsey fringe pulse, we insert an additional π operation at the center of $t_{\rm wait}$ to construct the Hahn-echo pulse. The π pulse will cancel the phase error that accumulates during the former and the latter wait time $t_{\rm wait}/2$. Figure 3(d) plots the Hahn-echo signal, and the coherence time is improved to 191.96 μs.

5. Electric field dependence of three-electron qubit

Since the explanation for thermally populated process does not make sense, we confirm the electric field dependence of the upper valley state via the three-electron qubit resonance frequency $f_{\text{res-3e}}$. Like the measurement process of one-electron qubit shown in Fig. 2(d), we choose $(2,0)$–$(3,0)$ charge transition as the working area. Figure 4(a) shows the electric field dependence of $f_{\text{res-3e}}$, where the base frequency is $f_{\text{res-3e}} = 26.0385$ GHz. Here, the electric field dependence $\alpha_{3\rm e}$ is -29.79 MHz/V which is comparable to $\alpha_{\rm U} = -26.21$ MHz/V shown in Fig. 2(d), and the sign is the same as that of $\alpha_{\rm U}$. Therefore, we emphasize that the bimodal EDSR signal in Fig. 2(a) arises from the spin flip of the electron that occupies the ground valley or the upper valley state. However, the mechanism that one electron occupies the upper valley state in Si-MOS QD platform remains to be understood. In Fig. 4(b), we demonstrate the three-electron qubit control. The Rabi frequency $f_{\text{Rabi-3e}}$ of the three-electron qubit is 1.356 MHz at $P = 20$ dBm, which is slower than that of the one-electron qubit at $P = 15$ dBm. We list two main reasons to explain the acceptable qubit control properties. From one electron to three electrons, the QD location may change, resulting in a change of the magnetic field gradient which is proportional to the qubit control speed. The other is the different MW response for one-electron and three-electron qubits.

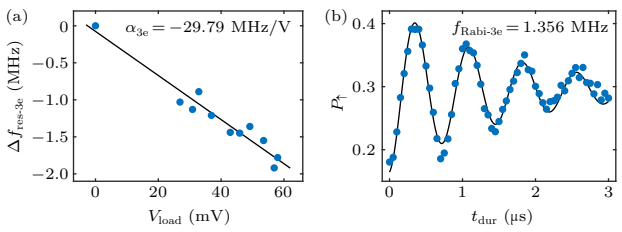


Fig. 4. (a) Electric field dependence of $f_{3\rm e}$ with $\alpha_{3\rm e} = -29.79$ MHz/V, which is comparable with the result shown in Fig. 2(d). (b) Electron spin up probability $P_\uparrow$ as a function of $t_{\rm dur}$ at $P = 20$ dBm. The three-electron qubit Rabi frequency $f_{\text{Rabi-3e}}$ of 1.356 MHz is extracted.

6. Conclusion

We measure the electric and magnetic field dependence of the qubit resonance frequency that occupies the ground or upper valley states in an isotopically enriched silicon quantum dot device. The relative difference of g-factor is approximately 0.0676%, and the difference of electric field dependence is 52.02 MHz/V. We further show the qubit control and coherence properties. The Rabi frequency of 2.804 MHz is achieved, and the dephasing time is approximately 1.084 μs, which can be enlarged to 191.96 μs by using dynamic decoupling protocol. The power dependence of Rabi frequency and quality factor are characterized to realize suitable qubit control. By combining with the electrical tunability of qubit resonance frequency and sequential encoding of an electron spin qubit in the ground and upper valleys, the qubit addressability, individual single-qubit control and two-qubit gate approaches can be easily realized, which is a potential approach to achieve scalable quantum computing.

Appendix A: Electron temperature and valley splitting

Figure A1(a) plots the unfilled probability of the first electron in MD as a function of the M gate voltage. Based on the Fermi–Dirac function and the extracted level arm, the electron temperature T_e is approximately 258.4 mK, corresponding to the thermal energy of 22.3 μeV.

The magnetospectroscopy of the third electron filling in LD is shown in Fig. A1(b). When the Zeeman energy E_Z is smaller than the valley splitting E_{vs}, the third electron will fill the spin down state of upper valley. Otherwise, the third electron will fill the spin up state of the ground valley. Figure A1(c) shows the energy level diagram of the first four electron fills in LD, where the black dashed lines marked the energy occupation of the third electron. Therefore, the tipping point in Fig. A1(b) represents $E_Z = E_{vs}$, where the external magnetic field is approximately 2.6 T. After taking the MM magnetic field component parallel to B_{ext} into account (approximately 50 mT), E_{vs} is 327.3 μeV.

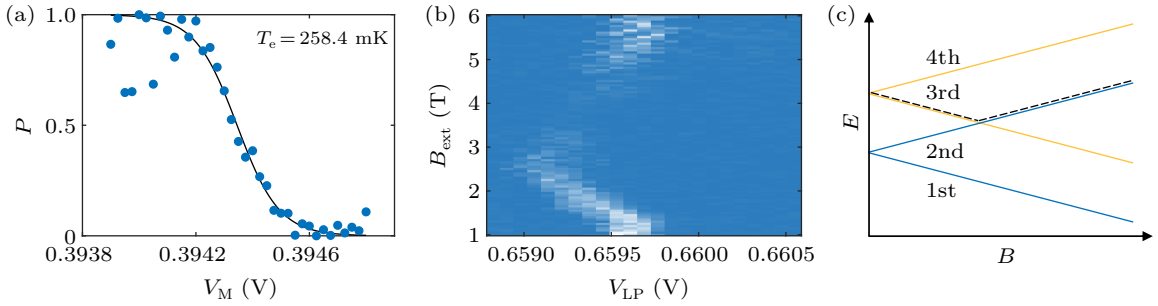


Fig. A1. (a) Time-averaged quantum dot occupation. The electron temperature T_e is approximately 258.4 mK, corresponding to the thermal energy of 22.3 μeV. (b) Magnetospectroscopy of the third electron filling in LD, where the tipping point represents $E_Z = E_{vs}$. Here, E_{vs} is approximately 327.3 μeV. (c) The energy levels of the two lowest valley states to explain the third electron filling in QD. As the strength of the magnetic field increases, the black dashed line marks the energy occupation of the third electron.

Acknowledgments

Project supported by the National Natural Science Foundation of China (Grant Nos. 12074368, 92165207, 12034018, and 92265113), the Innovation Program for Quantum Science and Technology (Grant No. 2021ZD0302300), the Anhui Province Natural Science Foundation (Grant No. 2108085J03) and the USTC Tang Scholarship. This work was partially carried out at the USTC Center for micro and nanoscale research and fabrication.

References

[1] Loss D and DiVincenzo D P 1998 *Phys. Rev. A* **57** 120
[2] Hanson R, Kouwenhoven L P, Petta J R, Tarucha S and Vandersypen L M 2007 *Rev. Mod. Phys.* **79** 1217
[3] Zhang X, Li H O, Wang K, Cao G, Xiao M and Guo G P 2018 *Chin. Phys. B* **27** 020305
[4] Wang K, Li H O, Xiao M, Cao G and Guo G P 2018 *Chin. Phys. B* **27** 090308
[5] Zhang X, Li H O, Cao G, Xiao M, Guo G C and Guo G P 2019 *Natl. Sci. Rev.* **6** 32
[6] Tyryshkin A M, Tojo S, Morton J J, *et al.* 2012 *Nat. Mater.* **11** 143
[7] Zwerver A, Krähenmann T, Watson T, *et al.* 2022 *Nat. Electron.* **5** 184
[8] Neyens S, Zietz O, Watson T, *et al.* 2024 *Nature* **629** 80
[9] Ha W, Ha S D, Choi M D, *et al.* 2021 *Nano Lett.* **22** 1443
[10] Camenzind L C, Geyer S, Fuhrer A, Warburton R J, Zumbühl D M and Kuhlmann A V 2022 *Nat. Electron.* **5** 178
[11] Veldhorst M, Hwang J, Yang C, *et al.* 2014 *Nat. Nanotechnol.* **9** 981
[12] Yoneda J, Takeda K, Otsuka T, *et al.* 2018 *Nat. Nanotechnol.* **13** 102
[13] Xue X, Russ M, Samkharadze N, Undseth B, Sammak A, Scappucci G and Vandersypen L M 2022 *Nature* **601** 343
[14] Noiri A, Takeda K, Nakajima T, Kobayashi T, Sammak A, Scappucci G and Tarucha S 2022 *Nature* **601** 338
[15] Mills A R, Guinn C R, Gullans M J, Sigillito A J, Feldman M M, Nielsen E and Petta J R 2022 *Sci. Adv.* **8** eabn5130
[16] Takeda K, Noiri A, Nakajima T, Kobayashi T and Tarucha S 2022 *Nature* **608** 682
[17] Phillips J 1962 *Phys. Rev.* **125** 1931
[18] Ando T, Fowler A B and Stern F 1982 *Rev. Mod. Phys.* **54** 437
[19] Zwanenburg F A, Dzurak A S, Morello A, Simmons M Y, Hollenberg L C, Klimeck G, Rogge S, Coppersmith S N and Eriksson M A 2013 *Rev. Mod. Phys.* **85** 961
[20] Yang C, Rossi A, Ruskov R, Lai N, Mohiyaddin F, Lee S, Tahan C, Klimeck G, Morello A and Dzurak A 2013 *Nat. Commun.* **4** 2069
[21] Eriksson M A, Friesen M, Coppersmith S N, Joynt R, Klein L J, Slinker K, Tahan C, Mooney P, Chu J and Koester S 2004 *Quantum Inform. Process.* **3** 133
[22] Saraiva A, Calderón M, Capaz R B, Hu X, Sarma S D and Koiller B 2011 *Phys. Rev. B* **84** 155320

[23] Kawakami E, Scarlino P, Ward D R, Braakman F, Savage D, Lagally M, Friesen M, Coppersmith S N, Eriksson M A and Vandersypen L 2014 *Nat. Nanotechnol.* **9** 666

[24] Culcer D, Saraiva A, Koiller B, Hu X and Sarma S D 2012 *Phys. Rev. Lett.* **108** 126804

[25] Schoenfield J S, Freeman B M and Jiang H 2017 *Nat. Commun.* **8** 64

[26] Penthorn N E, Schoenfield J S, Rooney J D, Edge L F and Jiang H 2019 *NPJ Quantum Inf.* **5** 94

[27] Corna A, Bourdet L, Maurand R, *et al.* 2018 *NPJ Quantum Inf.* **4** 6

[28] Klemt B, El-Homsy V, Nurizzo M, *et al.* 2023 arXiv:2303.04960 [cond-mat.mes-hall]

[29] Huang P and Hu X 2014 *Phys. Rev. B* **90** 235315

[30] Zhang X, Hu R Z, Li H O, *et al.* 2020 *Phys. Rev. Lett.* **124** 257701

[31] Scarlino P, Kawakami E, Jullien T, Ward D, Savage D, Lagally M, Friesen M, Coppersmith S, Eriksson M and Vandersypen L 2017 *Phys. Rev. B* **95** 165429

[32] Hansen I, Seedhouse A E, Chan K W, Hudson F, Itoh K M, Laucht A, Saraiva A, Yang C H and Dzurak A S 2022 *Appl. Phys. Rev.* **9** 031409

[33] Laucht A, Muhonen J T, Mohiyaddin F A, *et al.* 2015 *Sci. Adv.* **1** e1500022

[34] Xiong H, Ficheux Q, Somoroff A, Nguyen L B, Dogan E, Rosenstock D, Wang C, Nesterov K N, Vavilov M G and Manucharyan V E 2022 *Phys. Rev. Res.* **4** 023040

[35] Petit L, Russ M, Eenink G H, Lawrie W I, Clarke J S, Vandersypen L M and Veldhorst M 2022 *Commun. Mater.* **3** 82

[36] Zajac D, Hazard T, Mi X, Wang K and Petta J R 2015 *Appl. Phys. Lett.* **106** 223507

[37] Dodson J, Holman N, Thorgrimsson B, Neyens S F, MacQuarrie E, McJunkin T, Foote R H, Edge L, Coppersmith S and Eriksson M 2020 *Nanotechnology* **31** 505001

[38] Hu R Z, Ma R L, Ni M, *et al.* 2021 *Nanomaterials* **11** 2486

[39] Hu R Z, Ma R L, Ni M, *et al.* 2023 *Appl. Phys. Lett.* **122** 134002

[40] Ma R L, Li A R, Wang C, *et al.* 2024 *Phys. Rev. Appl.* **21** 014044

[41] Elzerman J, Hanson R, Willems van Beveren L, Witkamp B, Vandersypen L and Kouwenhoven L P 2004 *Nature* **430** 431

[42] Morello A, Pla J J, Zwanenburg F A, *et al.* 2010 *Nature* **467** 687

[43] Hu R Z, Zhu S K, Zhang X, *et al.* 2023 *Chin. Phys. B* **33** 010304

[44] Pioro-Ladriere M, Obata T, Tokura Y, Shin Y S, Kubo T, Yoshida K, Taniyama T and Tarucha S 2008 *Nat. Phys.* **4** 776

[45] Zhang X, Zhou Y, Hu R Z, *et al.* 2021 *Phys. Rev. Appl.* **15** 044042

[46] Yang C, Lim W, Lai N, Rossi A, Morello A and Dzurak A 2012 *Phys. Rev. B* **86** 115319

[47] Zhao R, Tanttu T, Tan K Y, *et al.* 2019 *Nat. Commun.* **10** 5500

[48] Barnes E, Kestner J, Nguyen N and Sarma S D 2011 *Phys. Rev. B* **84** 235309

[49] Veldhorst M, Ruskov R, Yang C, Hwang J, Hudson F, Flatté M, Tahan C, Itoh K M, Morello A and Dzurak A 2015 *Phys. Rev. B* **92** 201401

[50] Zajac D M, Sigillito A J, Russ M, Borjans F, Taylor J M, Burkard G and Petta J R 2018 *Science* **359** 439

[51] Tokura Y, van der Wiel W G, Obata T and Tarucha S 2006 *Phys. Rev. Lett.* **96** 047202

[52] Friesen M and Coppersmith S 2010 *Phys. Rev. B* **81** 115324

[53] Gamble J K, Eriksson M, Coppersmith S and Friesen M 2013 *Phys. Rev. B* **88** 035310

[54] Scarlino P, Kawakami E, Ward D, Savage D, Lagally M, Friesen M, Coppersmith S, Eriksson M and Vandersypen L 2015 *Phys. Rev. Lett.* **115** 106802